A Novel APP p.V742L variant in a patient with ischemic small vessel disease enhances FE65 signalling

Voesenek, B.J.B.; Rutten, J.W.; Mulder, M.P.C.; Mei, H.L.; Nibbeling, E.A.R.; Etten, E.S. van; ... ; Buijsen, R.A.M.

Neurobiology of Disease 220 (2026) 107280

Contents lists available at ScienceDirect

Neurobiology of Disease

journal homepage: www.elsevier.com/locate/ynbdi

A Novel APP p.V742L variant in a patient with ischemic small vessel disease enhances FE65 signalling

Bas J.B. Voesenek [a], Julie W. Rutten [b], Monique P.C. Mulder [c], Hailiang Mei [d], Esther A.R. Nibbeling [b], Ellis S. van Etten [e], Willeke M.C. van Roon-Mom [a], Saskia A.J. Lesnik Oberstein [b], Elena Daoutsali [a,f,1], Ronald A.M. Buijsen [a,1,*]

[a] Department of Human Genetics, Leiden University Medical Center, 2333 ZC Leiden, the Netherlands
[b] Department of Clinical Genetics, Leiden University Medical Center, 2333 ZA Leiden, the Netherlands
[c] Department of Cell and Chemical Biology, Leiden University Medical Center, 2333 ZC Leiden, the Netherlands
[d] Department of Biomedical Data Sciences, Leiden University Medical Center, 2333 ZC Leiden, the Netherlands
[e] Department of Neurology, Leiden University Medical Center, 2333 ZA Leiden, the Netherlands
[f] Department of Translational Neuroscience, University Medical Center Utrecht Brain Center, Utrecht University, Utrecht, the Netherlands

ARTICLE INFO

Keywords:
APP
AICD
Ischemic stroke
Lysosomes
FE65

ABSTRACT

Pathogenic variants in the amyloid precursor protein gene (*APP*) have been linked to Alzheimer's disease and intracerebral haemorrhage resulting from cerebral amyloid angiopathy. In these disorders, variants are generally located within or surrounding the amyloid-beta domain of *APP* and mostly increase the production or aggregation properties of the toxic amyloid-beta peptide. Here, we report a novel APP p.V742L variant in the APP intracellular domain (AICD) in a patient with a clinical and neuroradiological ischemic small vessel disease phenotype and a positive family history. We investigate the functional consequences of the variant on AICD function.

We obtained patient fibroblasts through a skin biopsy and applied immunocytochemistry to examine the subcellular localization of APP. Subsequently, 3' mRNA sequencing was deployed to investigate changes in gene expression. Finally, the effect of the variant on the binding of FE65 to AICD was investigated using co-immunoprecipitation followed by western blot.

Localization of APP p.V742L to lysosomes was increased, without affecting lysosomal motility. Transcriptome analysis showed altered expression of AICD target genes as well as dysregulation of genes relevant to the ischemic stroke phenotype. Finally, APP p.V742L was associated with an increased interaction with FE65, its most important intracellular binding partner.

Taken together, our data demonstrate that the APP p.V742L variant enhances the interaction of the AICD with FE65, resulting in dysregulation of gene transcription. This study illustrates the diverse roles of APP in brain disorders, and suggests ischemic small vessel disease as a novel APP-associated phenotype.

1. Introduction

The amyloid precursor protein (*APP*) gene is well known for its causal involvement in Alzheimer's disease and cerebral amyloid angiopathy (Greenberg et al., 2020). This type I transmembrane glycoprotein is ubiquitously expressed in most tissues, with its levels peaking in the brain (Uhlén et al., 2015). APP is processed through consecutive cleavage by α-, β- and γ-secretases leading to the generation of multiple fragments including soluble APP fragments, amyloid-beta (Aβ), and the APP intracellular domain (AICD) (Haass et al., 2012). These APP fragments are thought to be involved in a wide range of processes in both the developing as well as the adult brain, including neuronal development, synaptic function and plasticity, neuromuscular junction formation, neuroprotection, and preservation of cerebrovascular function (Cho et al., 2022; Müller et al., 2017; Katusic et al., 2025).

Numerous pathogenic *APP* variants have been linked to early-onset

* Corresponding author at: Einthovenweg 20, 2333 ZC, Leiden, the Netherlands.
E-mail address: r.a.m.buijsen@lumc.nl (R.A.M. Buijsen).
[1] These authors contributed equally to this work.

https://doi.org/10.1016/j.nbd.2026.107280
Received 7 October 2025; Received in revised form 22 December 2025; Accepted 19 January 2026
Available online 25 January 2026

Alzheimer's disease, early-onset haemorrhages due to genetic subtypes of cerebral amyloid angiopathy, or both (Greenberg et al., 2020). These mutations are located almost exclusively inside or around the Aβ domain and result in altered APP processing and/or accumulation of Aβ in the brain parenchyma (in Alzheimer's disease) or along blood vessel walls (in cerebral amyloid angiopathy) (Greenberg et al., 2020). So far, only three pathogenic variants (p.L723P, p.K724M, and p.K724N) have been identified in the AICD and were all found in patients with early-onset Alzheimer's disease. The p.L723P variant is located on the final residue of the transmembrane region of APP, while p.K724M and p.K724N are located on the first cytosolic residue (Kwok et al., 2000; Peng et al., 2014; Theuns et al., 2006). All three variants have been reported to increase the production of the Aβ42 peptide that is involved in early events in the pathogenesis of Alzheimer's disease, while APP p.L723P has also been reported to induce apoptosis (Kwok et al., 2000).

In contrast to previously identified *APP* variants, we identified a variant in the AICD that likely is associated with familial ischemic brain small vessel disease. This APP p.V742L variant is within the ^{742}VTPEER^{747} motif of the AICD and is adjacent to threonine 743 (T743), a crucial neuron-specific phosphorylation site that influences the 3-dimensional conformation of the AICD (Ramelot and Nicholson, 2001). This conformation determines accessibility of other AICD motifs, such as the ^{757}YENPTY^{762} motif that forms a docking site for FE65 to regulate a wide range of AICD functions including gene transcription (Ng et al., 2024; Chang et al., 2006). T743 phosphorylation also regulates intracellular trafficking of APP and exhibits clinical significance, as enhanced T743 phosphorylation is observed in Alzheimer's disease (Lee et al., 2003).

In the current study, we investigated the functional consequences of the APP p.V742L variant in patient-derived fibroblast cells. We examined APP subcellular localization and observed increased abundance of APP p.V742L in lysosomes. In addition, we performed gene expression analysis and studied the interaction between AICD and FE65. We found that the APP p.V742L variant alters downstream nuclear signalling, possibly resulting from increased affinity for FE65.

2. Materials and methods

2.1. Whole exome sequencing

Genomic DNA (gDNA) was extracted from blood following clinically standardized procedures. gDNA was used for whole exome sequencing (WES) which was performed using SureSelectXT Human All Exon v7 (Agilent) and sequenced on an Ilumina platform to achieve a mean coverage of 30×. Read alignment and variant calling were performed with the DRAGEN Germline pipeline v4.0.3 (Ilumina). Variant analysis was performed using Franklin software (Qiagen).

2.2. Fibroblast culture

A 4 mm skin biopsy punch was obtained from the lateral upper arm of the patient with the APP p.V742L variant. After dissection of the biopsy, fibroblasts were cultured in Minimum Essential Medium with Earle's Salts and Non Essential Amino Acids, without L-Glutamine (Gibco, cat#10370021) supplemented with 15% Foetal Bovine Serum (FBS), 2 mM GlutaMAX Supplement (Thermo Scientific, cat#35050038), and 1× Penicillin-Streptomycin. Cell lines were maintained in 37 °C and 5% CO_2. For cryopreservation, fibroblasts were washed with Dulbecco's phosphate-buffered saline (dPBS, Gibco, cat#14190144) and harvested after 5-min incubation with 1× trypsin. The suspension was centrifuged for 5 min at 1200 rpm, after which supernatant was removed and the cell pellet was resuspended in 10% DMSO, 20% FBS, in Dulbecco's Modified Eagle Medium (DMEM, cat#11965092) for preservation in liquid nitrogen. Control fibroblasts were obtained from a previous study and cultured following the above described methods (Buijsen et al., 2023).

2.3. gDNA isolation cultured cells

Genomic DNA (gDNA) was isolated from fibroblasts using the ReliaPrep gDNA Tissue Miniprep System (Promega, cat#A2052). A modified version of the Protocol for Buccal Swabs was used, where the volumes of media were halved. In short, the cell pellet was dissolved in 200 µL PBS, 10 µL Proteinase K, and 200 µL Cell Lysis Buffer followed by vortexing and incubation at 56 °C for 30 min. Liquid was transferred to a column and washed three times with 500 µL Column Wash Solution, after which gDNA was collected in 25 µL nuclease-free water.

2.4. PCR

PCR was performed using the Roche FastStart Taq DNA Polymerase kit (Roche, cat#12032902001). PCR mix consists of isolated gDNA, 2 µl 10× buffer (with 20 mM MgCl2), 0.4 µl dNTPs (10 mM), 0.4 µl forward primer (10 pmol/ml), 0.4 µl reverse primer (10 pmol/ml), 0.2 µl FastStart Taq-polymerase (5 U/µl), and filled up to 20 µl with MilliQ (Supplementary Table 1). For amplification of APP exon 18 (APPex18), 200 ng gDNA was added to the PCR mix. For APOE exon 4 (APOEex4), 300 ng gDNA was used and 4 µl GC-rich solution was added to the PCR mix. PCR was performed on a Bio-Rad T100 Thermal Cycler (cat#1861096) using the following protocol for APPex18: 5 min at 95 °C, 40 cycles of [30 s 95 °C, 30 s 60 °C, 35 s 72 °C], and 7 min at 72 °C. The protocol for APOEex4 PCR was 4 min at 95 °C, 40 cycles of [20 s 95 °C, 30 s 55 °C, 45 s 72 °C], and 7 min at 72 °C. PCR product was cleaned up using the NucleoSpin Gel and PCR Clean-up kit (Macherey-Nagel, cat#740609.250) according to the manufacturers protocol.

2.5. Sanger sequencing

Sanger sequencing of gDNA extracted from fibroblasts was performed on a Applied Biosystems 96-capillary (ABI3730xl) system to confirm the presence of the *APP* variant and to determine the *APOE* genotype. Sanger sequencing mix consists of 1 µM primer and 200 ng PCR product in a total volume of 10 µl, according to the LGTC guidelines.

2.6. RNA isolation and RT-qPCR

RNA was isolated using the Reliaprep RNA Cell Miniprep System (Promega, cat# Z6012) according to the manufacturers protocol. RNA was collected in 30 µL nuclease-free water. RNA concentration was determined on a NanoDrop Spectrophotometer ND-1000 (Thermo Fisher Scientific).

Subsequently, the Transcriptor First Strand cDNA Synthesis Kit (Roche, cat#04897030001) was used to synthesize cDNA. In short, 150 ng RNA was added to 2 µl random hexamer primer and supplemented with MQ to a total volume of 13 µl. This mix was placed in a thermal block cycler for 10 min at 65C, followed by cooling on ice for 1 min. This template mix was supplemented with 4 µl 5× transcriptor RT Reaction Buffer, 0.5 µl Protector RNase Inhibitor (40 U/µl), 2 µl 10 mM dNTP's, and 0.5 µl Transcriptor Reverse Transcriptase. After mixing, the reagents were placed in a thermal block cycler according to the following protocol: 10 min at 25 °C, 30 min at 55 °C, and 5 min at 85 °C. Reaction was stopped by placing mix on ice.

For RT-qPCR, cDNA was diluted 10 times in MQ. SensiMix SYBR Hi-ROX (Meridian Bioscience, cat#QT605–05) was added in a 5:2 (SensiMix: cDNA) ratio. Primers were diluted in MQ to a concentration of 0.83 µM (Supplementary Table 1). For every qPCR reaction, 7 µl cDNA/SensiMix and 3 µl primer solution were pipetted. qPCR was performed on a LightCycler 480 System (Roche Diagnostics).

2.7. Protein isolation and western blot

Protein was isolated by resuspending the cell pellet in RIPA buffer

(50 mM Tris-HCl pH 8.0, 150 mM NaCl, 1% IGEPAL CA-630, 0.5% DOC, 0.1% SDS, in MilliQ) supplemented with cOmplete EDTA-free protease inhibitors (Roche, cat#11873580001) followed by incubation on ice for 30 min with vortexing every 5 min. Cells were centrifuged for 10 min at 10.000 rpm in 4 °C. Supernatant was collected, supplemented with 5% glycerol and stored in the freezer until further use.

Protein concentration was determined using the Pierce BCA Protein Assay Kit (Pierce, cat#23225). In short, isolated protein was diluted, supplemented with Working Reagent and incubated at 37 °C for 30 min. Absorbance was measured at 562 nm using the SpectraMax iD3 Microplate Reader (Molecular Devices).

Twenty five ug protein sample was loaded on a 4–12% Bis-Tris gel with 1× MOPS SDS running buffer and transferred to a nitrocellulose membrane using the Trans-Blot Turbo Transfer System (Bio-Rad, cat#1704150). Membranes were blocked for 1 h at RT with 5% milk powder in TBS-T and stained with primary antibodies for FE65 (Invitrogen, cat#MA5–37408) or APP (Abcam, cat#ab32136) and secondary IRDye 680 and IRDye 800 antibodies for imaging on the Odyssey CLx Imager (LI-CORbio) (Supplementary Table 2). For normalization of APP protein levels on western blot, the nitrocellulose membrane was stained with Revert™ Total Protein Stain followed by two washes with washing solution (6.7% glacial acetic acid, 30% methanol, in water) and imaging on the Odyssey CLx Imager prior to blocking. Data was analyzed in Image Studio Lite (LI-CORbio, v5.2).

2.8. Immunocytochemistry and confocal microscopy

Fibroblasts were plated in a 12-well plate with a density of 100.000 cells per well on coverslips. The next day, cells were fixated with 4% paraformaldehyde (PFA) and washed with PBS. The plates were sealed with parafilm and stored in the fridge until immunostainings were performed.

Immunocytochemistry was performed to determine subcellular localization of APP and its C-terminal fragments to early endosomes, trans-Golgi network, endoplasmic reticulum, and lysosomes (Supplementary Table 2). Cells were incubated with immunobuffer (0.1% triton in 1× PBS + 1% horse serum +0.04% Merthiolate) for 30 min at room temperature. Primary antibody treatment was performed overnight in 4 °C, followed by washing in PBS. Subsequently, cells were incubated with secondary antibodies for 3 h at room temperature. After washing in PBS, coverslips were transferred to a microscopy slide containing a droplet of Dako Mounting Medium (Agilent, cat#CS70330–2) and kept at room temperature overnight to dry. Microscopy slides were stored at 4 °C until confocal imaging was performed.

Confocal imaging was performed on a Leica SP8 confocal microscope. Prior to analysis, images with very dim or strong signal were removed. Images were analyzed with custom-designed scripts in Cell Profiler (v.4.2.5). Colocalization was quantified using Pearson's correlation.

2.9. Live cell imaging

For live imaging of lysosomes, LysoTracker Deep Red (cat#L12492, Invitrogen) was added to fibroblast culture medium in a 30.000× dilution (end concentration 33 nM) for 5 min, after which the medium was refreshed with medium without LysoTracker. Live imaging was performed on an Andor Dragonfly 500 inverted system linked to a Zyla sCMOS camera coupled with Fusion software (Andor). During imaging, samples were incubated at 37 °C with 5% CO_2 atmosphere. Images were taken with 200 ms interval and analyzed using the ImageJ (version 1.51w) TrackMate plugin (Ershov, et al., 2022 (Ershov et al., 2022), version 7.12.1).

3. RNA sequencing

Transcriptome analysis was performed on control versus patient fibroblast lines. Three technical replicates were submitted for CTR1 and patient fibroblasts, while one RNA sample was submitted for lines CTR2 and CTR3. Total RNA was isolated as described earlier under 'RNA isolation and RT-qPCR'. RNA quality was checked using the Bioanalyzer. Samples with an RIN (RNA Integrity Number) score of 9 or higher passed quality check for RNA-seq. 250 ng of total RNA was submitted to the LGTC, which performed 3` library prep and sequencing of the libraries using the Illumina NovaSeq 6000 150 bp paired-end with ~5 M reads/sample. RNAseq FASTQ files were processed using the opensource BIOWDL RNAseq pipeline v5.0.0 (https://zenodo.org/record/5109461#.Ya2yLFPMJhE) developed at the LUMC. This pipeline performs FASTQ preprocessing (including quality control, quality trimming, and adapter clipping), alignment, read quantification, and optionally transcript assembly. FastQC (v0.11.9) was used for checking raw read QC. Adapter clipping was performed using Cutadapt (v2.10) with the default settings. RNAseq reads' alignment was performed using STAR (v2.7.5a) on human reference genome GRCh38. umi_tools (v1.1.1) was used to remove duplicates identified by UMIs. The gene read quantification was performed using HTSeq-count (v0.12.4) with the Ensembl gene annotation version 111. Technical replicates were averaged prior to further analysis. Genes with a total read count lower than five over all samples were excluded from analysis. Data was subsequently normalized using the median of ratios method. Because our dataset is from the only known subject that is an APP p.V742L carrier, this represents the entire population and we do not have uncertainties in measured parameters, unlike one would normally have when investigating a sample of a population. This allows us to show *how* gene expression differs from controls, rather than applying statistics to determine *if* gene expression is different. Therefore, the SD of normalized counts in the control lines was calculated for each gene after which it was determined how many of these SDs fit between the mean expression of that gene in control and patient fibroblast lines (ΔSD). In addition, the Fisher's exact test was used to statistically identify differentially expressed genes, as done before for $n = 1$ RNA-seq experiments (Szepanowski et al., 2024). Combining these approaches, genes were considered significantly upregulated if the $\Delta SD > 5$ with Fisher's exact $p < 0.05$ and significantly downregulated if the $\Delta SD < 5$ with Fisher's exact $p < 0.05$. Gene ontology enrichment pathway analysis of significant terms was performed in DAVID (Sherman et al., 2022).

3.1. Preparation of biotinylated AICD peptides (REF, PAT and pREF) by solid-phase peptide synthesis (SPPS)

Peptides REF and the mutants pREF (T743D) and PAT (V742L) were synthesized using standard Fmoc-based solid-phase peptide synthesis (SPPS) protocols on a Syro II synthesizer (Multisyntech GmbH, Witten, Germany).

3.2. General procedure for PAT and REF peptides

SPPS was performed in syringes on a 5 μmol scale using preloaded Fmoc amino acid trityl resin (0.16 mmol/g, Rapp Polymere GmbH). Resin swelling was achieved by adding 1.25 mL *N*-methyl-2-pyrrolidone (NMP) for 5 min, repeated twice. Fmoc deprotection was carried out by treatment with 20% piperidine in NMP in three sequential steps of 3, 5, and 5 min, followed by five washes with NMP. Amino acid coupling was performed with a fourfold molar excess of Fmoc-protected amino acids in the presence of 4 equivalents benzotriazol-1-yloxytripyrrolidinophosphonium hexafluorophosphate (PyBOP) and 8 equivalents N,N-diisopropylethylamine (DiPEA) in NMP for 25 min. Coupling was done twice to ensure completeness, followed by three washing steps with NMP. After completion of the synthesis cycles, the resin was washed with diethyl ether (Et_2O) and dried under vacuum.

N-terminal biotinylation with a PEG_2 linker was performed by incubating the resin with 1 mL of NMP containing 20 μmol of 8-Biotinylamido-3,6-dioxaoctanoic acid dimer (Biotin-O2Oc-O2Oc-OH, CAS:

1301706–65-9, Iris Biotech GmbH), 20 μmol PyBOP, and 40 μmol DiPEA. The reaction mixture was incubated for 16 h at room temperature with shaking. After completion, the resin was washed sequentially with NMP, dichloromethane (DCM), and diethyl ether (Et_2O), then dried under high vacuum.

3.3. Modified procedure for pREF peptide

SPPS of the pPAT mutant was performed using the Syro II synthesizer equipped with a TIP module on a smaller scale (2 μmol) in tips. Resin swelling was conducted with 135 μL NMP for 5 min, repeated twice. Fmoc deprotection steps were identical to the general procedure (20% piperidine in NMP, 3 × 3, 5, and 5 min), followed by five washes with NMP. Amino acid coupling used the same fourfold excess of Fmoc amino acids, 4 equivalents PyBOP, and 8 equivalents DiPEA, but with an extended coupling time of 45 min per coupling step. Double coupling was applied as well, followed by three washes with NMP. The resin was then washed with Et_2O and dried under vacuum.

N-terminal biotinylation was performed by incubating the resin with 200 μL of NMP containing 8 μmol biotin (Biotin, CAS: 58–85-5, Sigma), 8 μmol PyBOP, and 16 μmol DiPEA. The mixture was incubated for 16 h at room temperature. Following coupling, the resin was washed with NMP, DCM, and Et_2O, and dried under high vacuum. To achieve the same PEG_2 spacer length as in Biotin-O2Oc-O2Oc-OH, two sequential couplings of Fmoc-8-amino-3,6-dioxaoctanoic acid (Fmoc-O2Oc-OH, CAS: 166108–71-0) were performed on the resin prior to biotin coupling. After each coupling, Fmoc deprotection was carried out as described above.

3.3.1. Global deprotection and cleavage

After synthesis and biotinylation, all peptides were cleaved from the resin and globally deprotected using a freshly prepared cocktail of TFA/H_2O/iPr_3SiH/phenol (90:5:2.5:2.5, *v*/v/v/v; 5 mL) for 3 h at room temperature under gentle shaking. The cleavage mixture was filtered, and peptides were precipitated in ice-cold Et_2O:n-pentane (3:1, *v*/v). The precipitate was collected by centrifugation (2 × 15 min, 3800 rpm, 4 °C), dissolved in H_2O:CH_3CN:formic acid (65:25:10, v/v/v), and lyophilized overnight. Peptides were purified by reverse-phase HPLC.

3.4. Pulldown with biotinylated AICD peptides

SH-SY5Y cells were cultured in 1:1 Minimum Essential Medium with Earle's Salts and Non Essential Amino Acids, without L-Glutamine (Gibco, cat#10370021)/Ham's F12 Nutrient Mix (Gibco, cat#11765054) supplemented with 10% Foetal Bovine Serum (FBS), 2 mM GlutaMAX Supplement, and 1× Penicillin-Streptomycin. One confluent 10 cm dish was used per pulldown. Cells were washed twice with ice-cold PBS prior to scraping in 1 ml cold lysis buffer (40 mM Tris-HCl, 150 mM KCl, 1% Igepal CA30, pH 7.4, supplemented with one tablet cOmplete Protease Inhibitor Cocktail (Roche) and one tablet PhosSTOP (Roche)). The obtained homogenates were incubated for 1 h at 4 °C under rotation, followed by centrifuging for 20 min at 16.000 *g* at 4 °C. Supernatant of two lysates were mixed and split in two for a co-IP with REF and PAT peptide to assure identical input for both peptides.

For pulldown experiments, 20 μg biotinylated peptide was incubated with 10 μL prewashed NeutrAvidin Agarose beaded resin (Thermo Scientific, cat#29202) for 3 h at 4 °C under rotation followed by four 8-min washes in 40 mM Tris-HCl, 0.1% BSA, pH 7.4. Beads were then equilibrated in 40 mM Tris-HCl, 150 mM KCl, 0.1% Igepal CA630, pH 7.4 and subsequently incubated with 850 μL lysate overnight. The next day, beads were washed four times in 40 mM Tris-HCl, 150 mM KCl, 0.1% Igepal CA630, pH 7.4 and two times in 40 mM Tris-HCl, 150 mM KCl, pH 7.4. All steps were performed at 4 °C. Samples were then eluted in 35 μL1× Bolt LDS Sample Buffer (Invitrogen cat#B0007) containing 1× Bolt Sample Reducing Agent (Invitrogen cat#B0009) and heated to 95 °C for 10 min. 20 μL of each sample was analyzed on western blot as described above.

3.5. Statistics

Statistics were performed in GraphPad Prism 10.2.3. Data is represented as mean ± SD. *p*-values lower than 0.05 were considered significant and are indicated with *. Statistical tests and results are mentioned in figure legends.

4. Results

4.1. Novel APP intracellular domain variant identified in a patient with cerebral ischemic small vessel disease

A 59-year old index patient was referred to the LUMC Expert Center for Genetic Cerebral Small Vessel Disease because of recurrent ischemic strokes and transient ischemic attacks (TIA's). She experienced three TIA's since the age of 50 and two ischemic strokes starting at the age of 56. She had a history of hypercholesterolemia and never smoked. Her medical history included a concussion four years prior, dysphagia six years prior, and post-concussion syndrome 14 years prior. Additionally, she had a history of carpal tunnel syndrome and cervicobrachialgia. Stroke workup revealed no evidence of carotid stenosis or large artery disease, and telemetry monitoring showed no abnormalities. Brain MRI was available at multiple timepoints in a 5 year period. These showed progressive symmetrical nodular and increasingly confluent white matter hyperintensities in the deep white matter, especially in the semioval centre and corona radiata, as well as extensive hyperintensities of the periventricular white matter on T2-weighted imaging. In the periventricular white matter there are several inlaying lacunar infarctions, with an additional larger lacune in the semioval centre at the second timepoint. No intracerebral haemorrhage and no microbleeds were seen on susceptibility weighted imaging (Fig. 1A-B, Supplementary Fig. 1).

The family history is suggestive of autosomal dominant inheritance of a predisposition for ischemic stroke, although reduced penetrance and variable expression cannot be ruled out (Fig. 1C). The patient's mother was reported to have a first stroke during pregnancy at age 43 years, and from age 56 years onwards she suffered from recurrent strokes and TIA's. She also had a history of breast cancer. She died at age 78 years. A maternal aunt reportedly had more than 10 strokes from age 50 years onwards. Her maternal grandfather had multiple strokes and died from a stroke at age 68 years. The patient has two brothers, neither of which had had ischemic strokes. The patient's father passed away during open heart surgery, at age 64 years. His family history was negative for strokes and dementia. The patient has one child, who has not had DNA testing. She is too young (under age 35 years) to be able to determine whether she has the stroke phenotype, as the onset of stroke in this family is above age 40 years.

Whole exome sequencing (WES) in the index patient showed a heterozygous *APP* c.2224G > C; p.(Val742Leu) (p.V742L, full length isoform) variant, located in exon 18 of the *APP* gene, encoding the C-terminal part of the APP intracellular domain (AICD) (Fig. 2A), and no other variants that could explain the patients phenotype. One of her healthy brothers, older than 75 years of age, had genetic testing and was shown not to harbour the APP p.V742L variant; the variant was also shown to be absent in a healthy >75 year old daughter of her maternal aunt.

The APP p.V742L variant was absent in genetic databases (Leiden Open-source Variation Database (Fokkema et al., 2021), UK Biobank (Bycroft et al., 2018), and GnomAD (Karczewski et al., 2020); accessed August 2025) and was predicted to be pathogenic by in silico prediction programs (DomScore 0.82, Maverick v1.1 (Danzi et al., 2023)). The variant is within a well-conserved domain, implying deleterious effects for missense variants on this residue (Fig. 2B). Since an ischemic small vessel disease phenotype has not been observed with *APP* variants

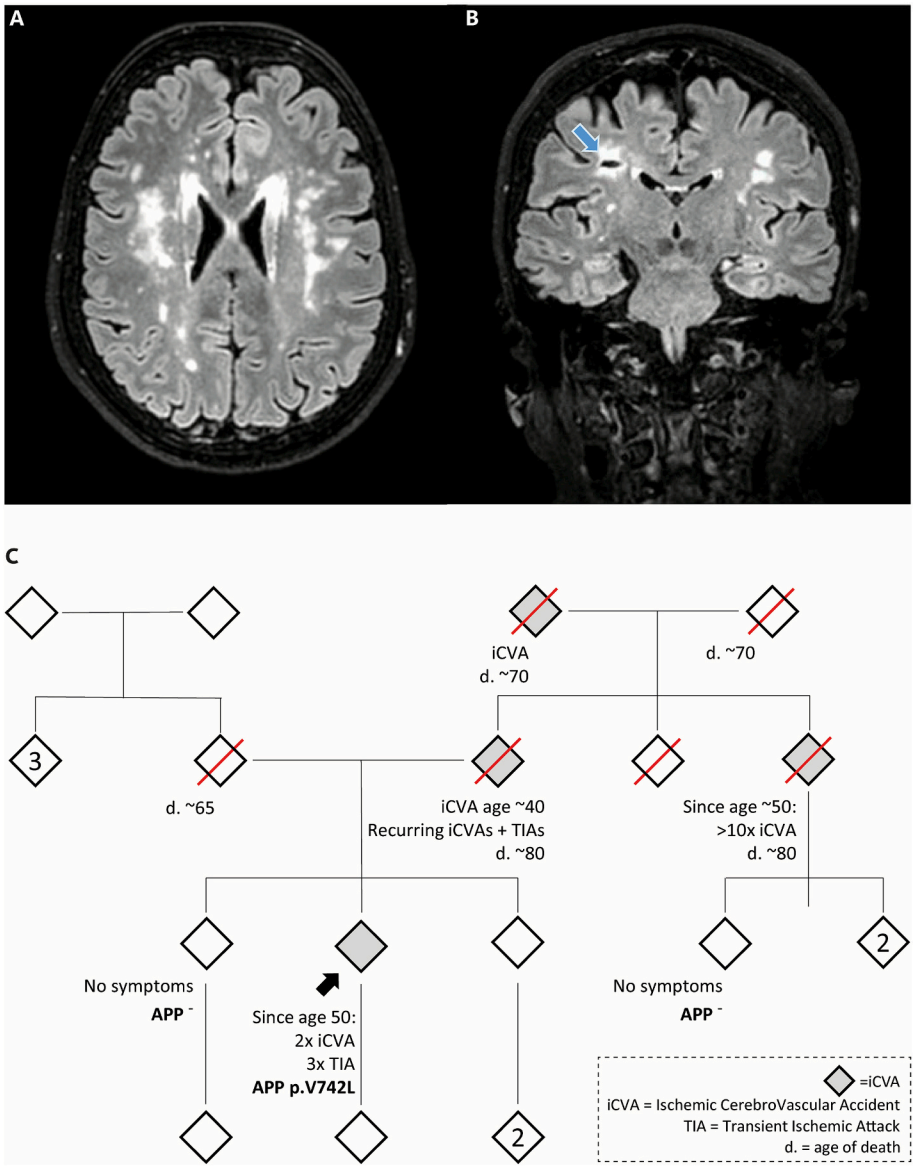

Fig. 1. White matter hyperintensities and lacunes in a patient with a positive family history for recurring ischemic strokes (A) Axial brain MRI FLAIR image at age 59 years showing symmetric deep and periventricular white matter hyperintensities. (B) Sagittal FLAIR image showing a lacune in the right semioval center (indicated by the arrow). No microbleeds or other hemorrhagic lesions were seen on SWI images (data not shown). Progression of MRI abnormalities is shown in Supplementary Fig. 1. (C) Pedigree of APP p.V742L patient showing a positive family history for strokes and TIA's (affected family members are indicated in grey). Number in diamond indicates number of siblings grouped for simplicity of the pedigree. A red line crossing a diamond indicates that this individual has deceased. (For interpretation of the references to colour in this figure legend, the reader is referred to the web version of this article.)

before, we obtained a skin biopsy from the patient to elucidate underlying mechanisms.

4.2. APP RNA and protein levels are unaltered in patient-derived fibroblasts

Fibroblasts from the patient and three unrelated age- and sex-matched controls were first deployed to study whether APP RNA and protein levels were affected by the p.V742L variant (Fig. 3A). Firstly, the presence of the *APP* variant in the patient fibroblast line was confirmed using Sanger sequencing (Fig. 3B). All cell lines were also screened for *APOE* genotype, revealing an APOE3/3 genotype for all cell lines except CTR3, which exhibited an APOE3/4 genotype. (Supplementary Fig. 2A-B). Subsequently, RNA levels of canonical *APP* isoforms were determined using RT-qPCR, revealing similar expression levels in patient and control fibroblasts (Fig. 3C-D). Accordingly, APP protein levels were found to be comparable in two independent experiments (Fig. 3E-F, Supplementary Fig. 3).

4.3. Increased abundance of C-terminal APP in lysosomes of patient fibroblasts

Although APP protein synthesis was not affected by the APP p.V742L variant, we examined whether its subcellular localization was altered. We hypothesized that the missense variant within the VTPEER motif could dysregulate intracellular sorting through modifying the 3-dimensional conformation of the AICD, thereby interfering with the access of its sorting motifs. Indeed, we observed increased APP localization with an antibody targeting the C-terminus of APP in lysosomes in patient fibroblasts, with significance reached compared to two out of three control fibroblast lines (Fig. 4A-H, Supplementary Fig. 4A-B). For the endoplasmic reticulum, trans-Golgi network, and early endosomes, APP

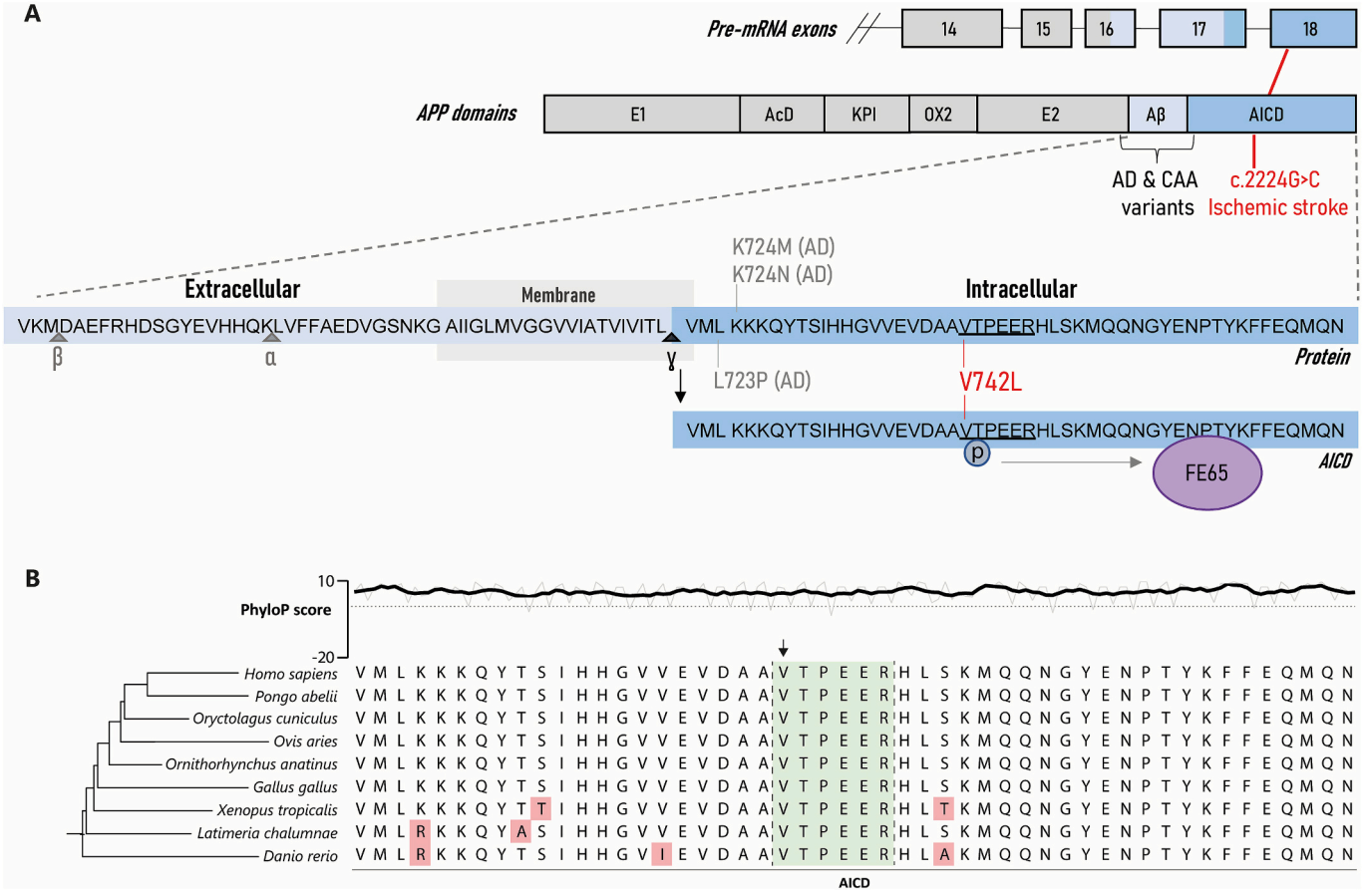

Fig. 2. Schematic overview and conservation of the amyloid precursor protein (APP) intracellular domain (AICD) (A) The APP p.V742L variant is located in exon 18, which encodes the C-terminal part of the AICD and is the most C-terminal APP variant found to date. It is within the VTPEER motif that regulates binding the AICD to FE65, it's most important interactor that for instance regulates gene transcription. Known pathogenic AICD variants were previously identified nearby the γ-secretase cleavage site and are associated with early-onset Alzheimer's disease (AD). (B) Amino acid sequence of the AICD in different species with PhyloP scores above. The APP p.V742L variant (position indicated with arrow) is located in the evolutionary well-conserved VTPEER motif (green boxes), as indicated by the positive PhyloP scores. Red boxes indicate a different amino acid compared to *Homo sapiens*. The grey graph shows PhyloP scores per nucleotide; the black plot shows smoothed PhyloP scores by applying four neighbouring points per side and second-order smoothing. (For interpretation of the references to colour in this figure legend, the reader is referred to the web version of this article.)

localization was found to be unaltered. Interestingly, it was recently shown that accumulation of APP C-terminal fragments in lysosomes hampers lysosomal motility (Bretou et al., 2024). Therefore, we deployed LysoTracker for the visualization and tracking of lysosomes in live cells (Fig. 4I, J, Supplementary Video 1). The lysosomal content was comparable in control and patient fibroblasts, but only a minority of these lysosomes was motile (~5.7%, Fig. 4K-L). To ensure that an effect of APP accumulation on lysosomal motility was not masked by this bulk analysis, we divided the lysosomal motility data into quartiles to investigate the impact of APP accumulation on fast- and slow-moving lysosomes independently. We did not observe any effects of APP accumulation on lysosomal displacement or displacement speed (Fig. 4L-N, Supplementary Fig. 4C-D). To summarize, patient fibroblasts show increased localization of APP to lysosomes without affecting lysosomal motility.

4.4. *Transcriptome analysis reveals dysregulation of disease-relevant genes in patient fibroblasts*

One of the most important functions of the AICD is regulating gene expression through its interaction with FE65 and TIP60 to form a transcriptionally active complex (Cao and Südhof, 2001). Using 3` mRNA sequencing (RNA-seq), we performed genome-wide gene expression analysis in control versus patient fibroblasts to identify dysregulated pathways that could potentially underly the ischemic stroke phenotype of the patient. For interpretation of the results, it is worth mentioning that WES revealed another pathogenic variant in the patient that increases the risk for breast and ovarian cancer, namely RAD51C: c.561_562del p.(His187Glnfs*15). Principal component analysis (PCA) showed clear clustering of replicates after normalization of the data (Supplementary Fig. 5A). We identified 186 up- and 52 downregulated genes in patient fibroblasts that were subsequently subject to DAVID pathway analysis (Sherman et al., 2022), only revealing significant enrichment of the Gene Ontology term 'Cytosol' (GO:0005829; Bonferroni-corrected $p = 0.0047$, Fig. 5A, Supplementary Fig. 5B). In addition, we explored the DisGeNET database within DAVID to find diseases linked to differentially expressed genes (DEGs) (Piñero et al., 2020). Interestingly, some of the DEGs in our dataset have previously been linked to cardiovascular disorders, including ischemia, although read counts were low and significance was not reached (Supplementary Fig. 6A).

As pathway analysis did not provide clear insights into the pathomechanism underlying the patient's ischemic cerebrovascular phenotype, we explored whether highly dysregulated genes from our dataset have previously been associated with APP or the vascular system in the literature (Table 1, Fig. 5B, validation of top hits in Supplementary Fig. 5C). Among the top 25 upregulated genes, several were related to APP interactors (*CCNG1* (Badhwar et al., *2017*)), APP metabolism

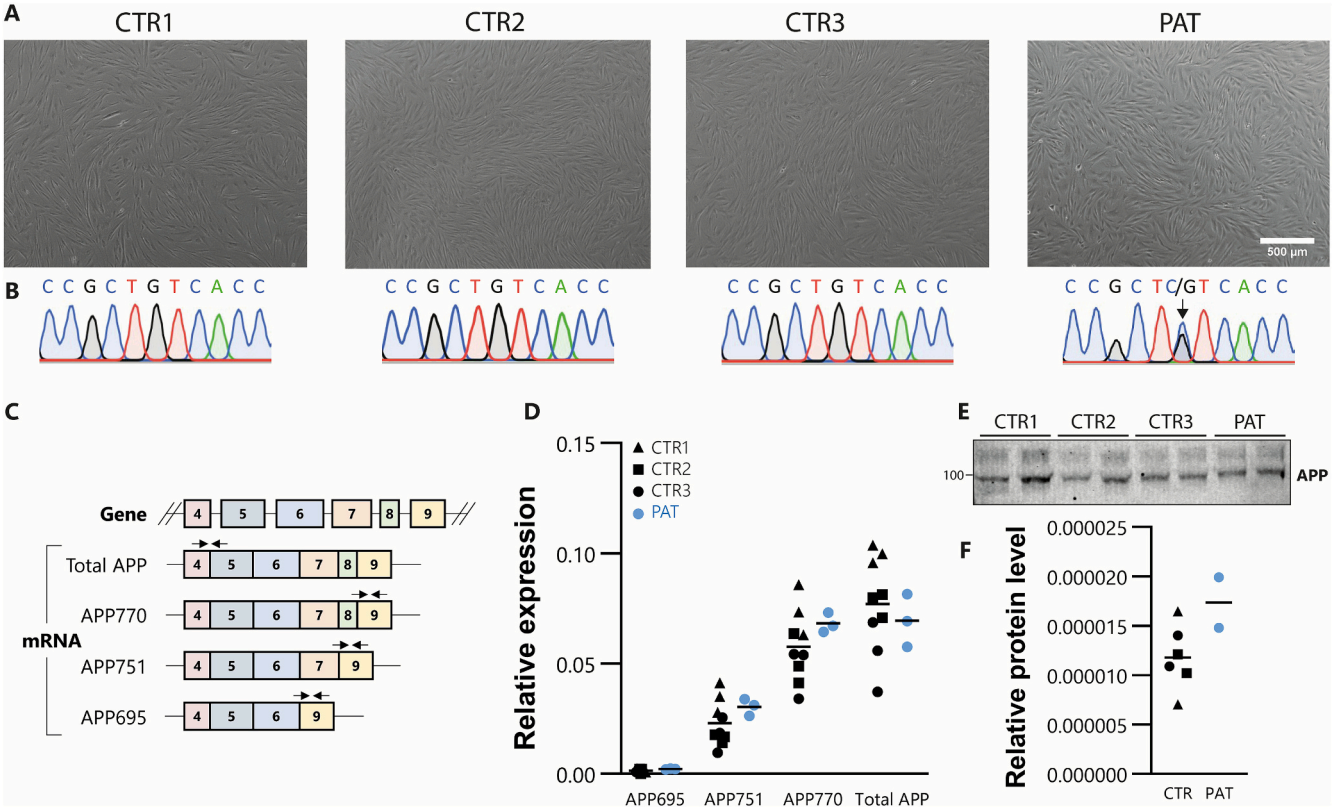

Fig. 3. Amyloid precursor protein (APP) expression is unaffected in patient-derived fibroblasts (A) Brightfield microscopy images of patient (PAT) and age- and sex-matched control fibroblasts (CTR1, CTR2 and CTR3). Scale bar is 500 µm. (B) Sanger sequencing shows the presence of the APP p.V742L variant in the patient line (indicated by the arrow) (C) Schematic representation of RT-qPCR primer design strategy. Boxes represent exons, arrows indicate location of forward and reverse primer. (D) RNA levels of canonical APP isoforms are unaltered in patient-derived fibroblasts (multiple unpaired *t*-tests, APP_{695} $p_{adj} = 0.4502$, APP_{751} $p_{adj} = 0.5916$, APP_{770} $p_{adj} = 0.5916$). (E) Western blot showing APP protein levels in control and patient fibroblasts. (F) Quantification of (E), APP protein levels are unaltered in patient fibroblasts (unpaired t-test, $p = 0.0851$). APP signal was normalized against TPS (Supplementary Fig. 3B).

(*SFRP2* (Esteve et al., *2011*), *CLU* (Kim et al., *2022*)), Alzheimer's disease (*HSP90AA1* (Astillero-Lopez et al., *2024*), *AMPH* (Bergström et al., *2021*), *GSTP1* (Vogrinc et al., *2023*), *S100A10* (King et al., *2020*), *PCP4* (Hu et al., *2023*), *CCNG1* (Badhwar et al., *2017*), *CLU* (Kim et al., *2022*)), CAA (*CLU* (Wojtas et al., *2017*; Bonaterra-Pastra et al., *2024*)), vascular integrity (*CDON* (Ahn et al., *2023*), *PDZRN3* (Sewduth et al., *2017*; Gueniot et al., *2022*), *HOXB5* (Fessner et al., *2014*)), and ischemic stroke risk (*HSP90AA1* (Kobzeva et al., *2024*)). The remaining 14 genes have not previously been linked to the relevant terms. Interestingly, just outside the top upregulated hits we observed *ADRA2A*, a receptor that directly interacts with the AICD and is known to induce vasoconstriction (Zhang et al., 2017; Hartmann et al., 2023; Tervi et al., 2024). Among the top 15 downregulated genes we found genes related to AICD interactors (*TLN1* (Ellis et al., *2024*)), APP interactors (*UCHL1* (Zhang et al., *2014*)), Alzheimer's disease (*UCHL1* (Zhang et al., *2014*), *BOK* (Yang et al., *2025*)), CAA (*TLN1* (Manousopoulou et al., *2020*)), Vascular integrity (*UCHL1* (Mitra et al., *2021*), *PDLIM5* (Hu et al., *2024*), *CCN3* (Shimoyama et al., *2010*), *MAGI1* (Abe et al., *2020*), *CREB3L1* (Zhao et al., *2022*), *CRIM1* (Glienke et al., *2002*), *LAMC1* (Buga et al., *2014*), *HOXC10* (Tan et al., *2018*)), and ischemic stroke risk (*LAMC1* (Surakka et al., *2023*), *GDF15* (Gan et al., *2025*)). Four genes were not linked to relevant terms. Taken together, transcriptomic analysis shows dysregulation of potential disease-relevant genes in patient fibroblasts.

4.5. *APP p.V742L variant interferes with FE65 binding*

The AICD regulates gene transcription through interacting with FE65 (Cao and Südhof, 2001). As RNA-seq analysis suggested possible transcriptional dysregulation in patient fibroblasts, we wondered whether the APP p.V742L variant interferes with FE65 binding. Due to the uncertainty about how phosphorylation of T743 influences the interaction with FE65, and given the lack of T743 phosphorylation in fibroblasts (Supplementary Fig. 6), we synthesized biotin-labelled AICD reference (REF), phosphomimic T743D (pREF), and patient variant V742L (PAT) peptide (Fig. 6A, Supplementary Fig. 7). Peptides REF and pREF were incubated with SH-SY5Y protein lysate and co-immunoprecipitated (co-IP) followed by analysis on western blot, which showed that FE65 binds preferentially to the unphosphorylated AICD peptide (REF) (Fig. 6C-D, Supplementary Fig. 8A). Next, we repeated the experiment with unphosphorylated REF and PAT peptide to compare their interaction with FE65. We found increased binding of FE65 to the PAT compared to the REF peptide in all replicate experiments (Fig. 6E-F, Supplementary Fig. 8B). As we did not observe decreased expression levels of FE65 in patient fibroblasts (Fig. 6G), our data indicates that the APP p.V742L variant enhances FE65 binding.

5. Discussion

In the current study, we report on a novel *APP* variant identified in a patient with ischemic cerebral small vessel disease and a positive family history suggesting an autosomal dominant pattern of inheritance. In patient-derived skin fibroblasts, we showed increased localization of APP in lysosomes and dysregulation of gene expression, presumably resulting from an enhanced interaction with FE65. This is the first described pathogenic *APP* variant that interferes with AICD-FE65 signalling.

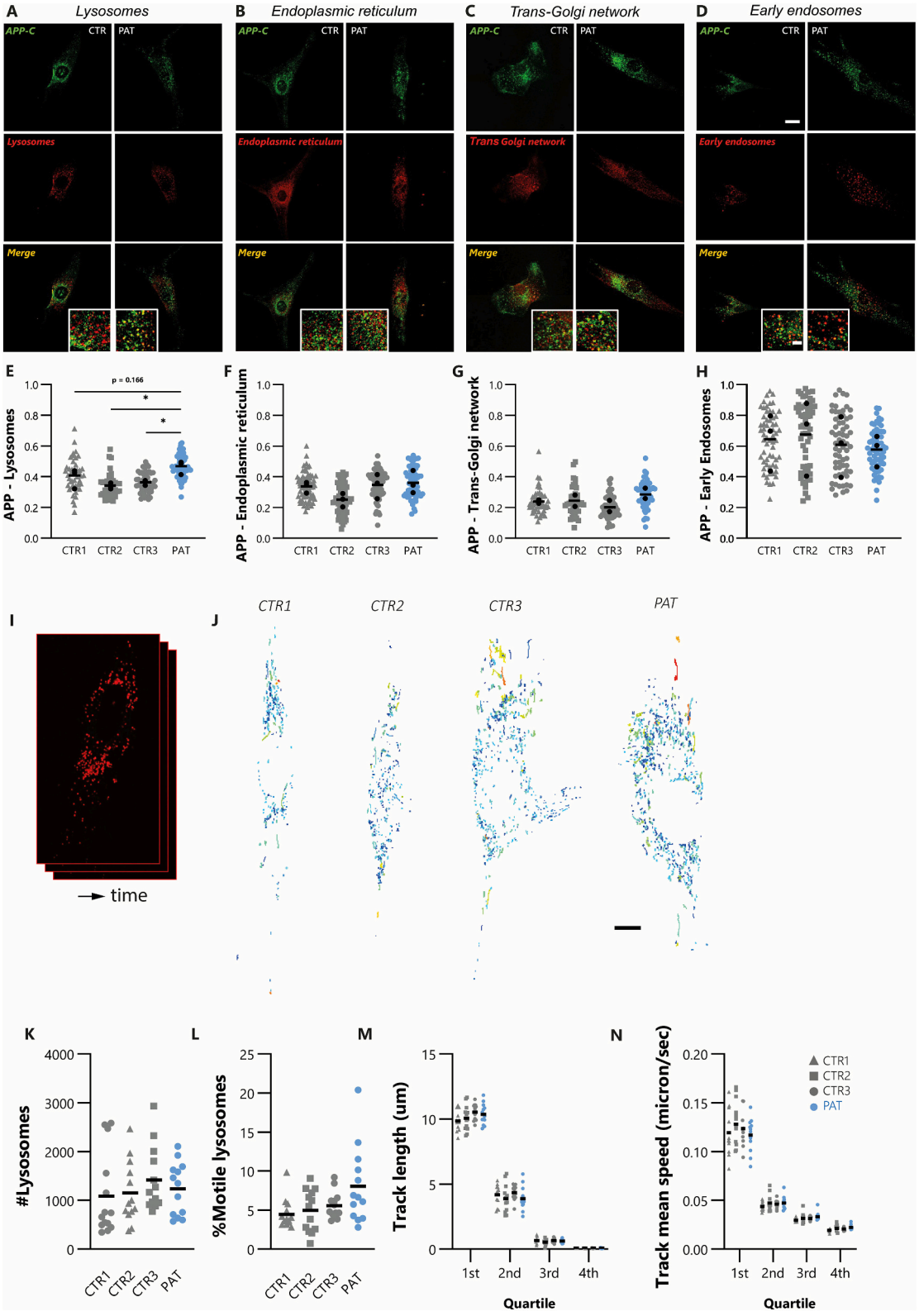

Fig. 4. Increased localization of APP p.V742L C-terminal fragments in lysosomes (A-D) Representative confocal images showing increased localization of APP (green) to lysosomes (A), endoplasmic reticulum (B), trans-Golgi network (C), or early endosomes (D) (red) in patient-derived fibroblasts. Scale bar is 25 μm. Boxes represent zoom in with a scale bar of 5 μm. (*E*-H) Quantification of colocalization in (A-D) showing increased localization of APP to lysosomes (One-Way ANOVA with Dunnett multiple comparison, $F_{3,8} = 5.372$, CTR1vsPAT $p = 0.2178$, CTR2vsPAT $p = 0.0124$, CTR3vsPAT $p = 0.0317$) and unaltered localization towards endoplasmic reticulum, trans-Golgi network, or early endosomes. (I) Example image of LysoTracker Deep Red labelling to examine lysosome movement in real time. (J) Example tracks showing the path travelled by lysosomes colour-coded for distance travelled. Scale bar 10 μm. (K) TrackMate analysis of LysoTracker live imaging revealing unaltered number of lysosomes in patient fibroblasts and (L) low fraction of motile lysosomes across all fibroblast lines. In fast- and slow-moving lysosomes, track length (M) and track mean speed (N) are comparable in control and patient fibroblasts. (For interpretation of the references to colour in this figure legend, the reader is referred to the web version of this article.)

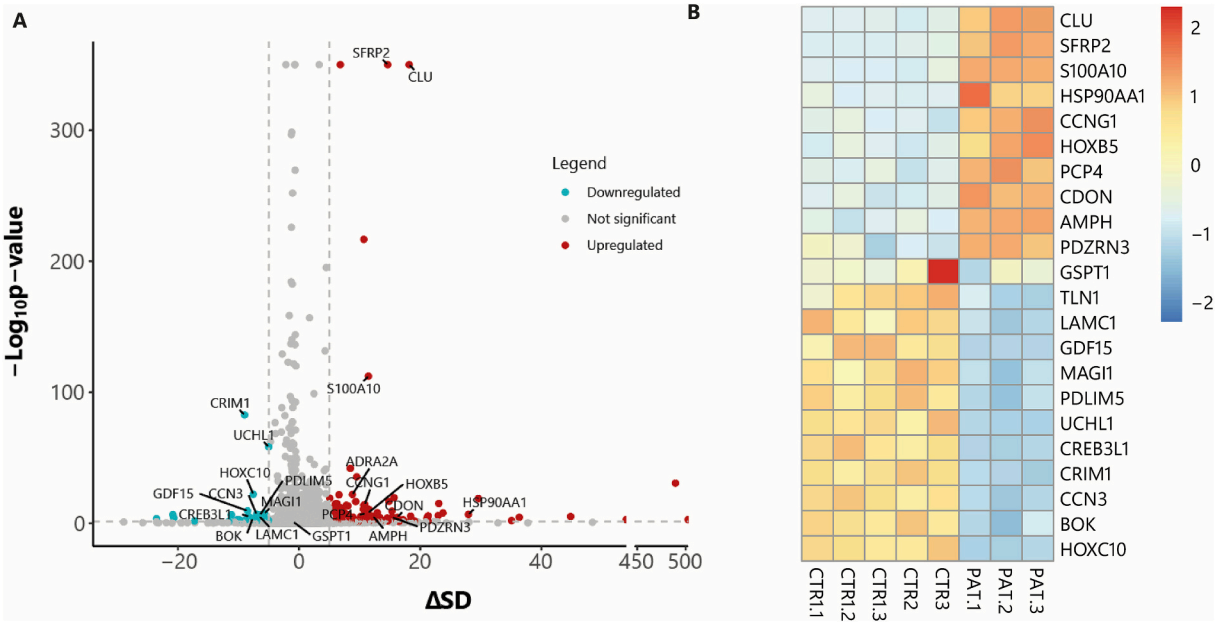

Fig. 5. Transcriptome analysis of APP p.V742L fibroblasts (A) Scatter plot showing genes differentially expressed as determined with the ΔSD (x-axis) and Fisher exact (y-axis) analyses. (B) Heatmap of the normalized reads in all replicate samples for the top 25 commonly upregulated and top 25 downregulated genes with a link to APP or the vascular system.

A

Peptide	Sequence
REF	Biotin-PEG-VMLKKKQYTSIHHGVVEVDAAVTPEERHLSKMQQNGYENPTYKFFEQMQN
pREF	Biotin-PEG-VMLKKKQYTSIHHGVVEVDAAVDPEERHLSKMQQNGYENPTYKFFEQMQN
PAT	Biotin-PEG-VMLKKKQYTSIHHGVVEVDAALTPEERHLSKMQQNGYENPTYKFFEQMQN

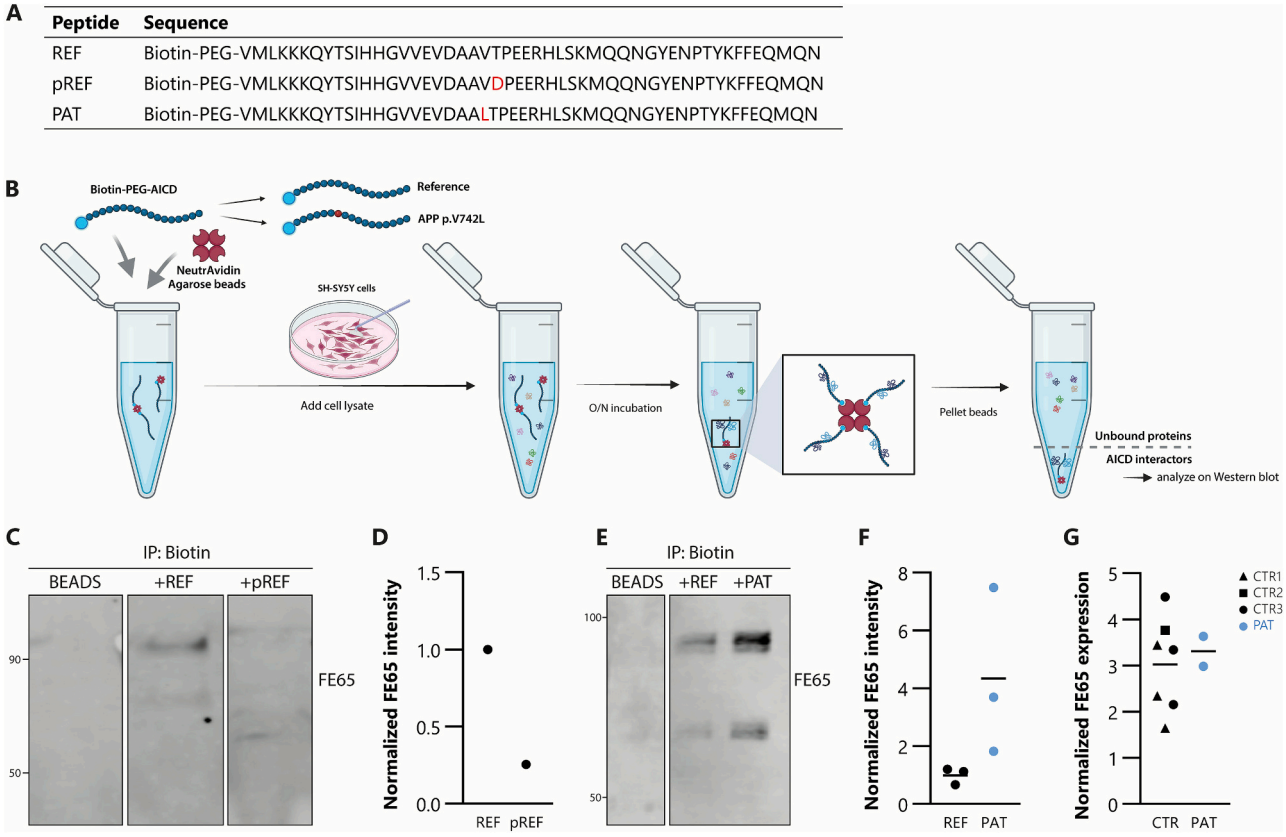

Fig. 6. The APP p.V742L variants enhances affinity of the AICD for FE65 (A) Sequences of synthetic AICD peptides. Amino acids in red indicate an alteration compared to the REF peptide. (B) Overview of co-immunoprecipitation workflow. (C) Western blot comparing the interaction of REF and pREF peptides for FE65. (D) Quantification of (C) showing strong affinity of REF compared to pREF peptide for FE65. (E) Western blot showing the interaction between FE65 and REF and PAT peptides. (F) Quantification of (E) revealing increased binding of FE65 to PAT peptide in all replicate experiments. (G) Normal FE65 expression in patient fibroblasts as measured by RT-qPCR (t-test, $p = 0.7187$). (For interpretation of the references to colour in this figure legend, the reader is referred to the web version of this article.)

Table 1
Classification of up- and downregulated genes into terms relevant to APP or ischemic strokes.

Term	Top 25 UP	Top 25 DOWN
AICD interactors		*TLN1*
APP interactors	*CCNG1*	*UCHL1*
APP metabolism	*SFRP2, CLU*	
Alzheimer's Disease	*HSP90AA1, AMPH, GSTP1, S100A10, PCP, CCNG1, CLU*	*UCHL1, BOK*
Cerebral Amyloid Angiopathy	*CLU*	*TLN1*
Vascular integrity	*CDON, PDZRN3, HOXB5*	*UCHL1, PDLIM5, CCN3, MAGI1, CREB3L1, CRIM1, LAMC1, HOXC10*
Ischemic stroke risk	*HSP90AA1*	*LAMC1, GDF15*

5.1. Pathogenic AICD variants in Alzheimer's disease cases

A pathogenic role for *APP* has been established before in early-onset Alzheimer's disease and genetic subtypes of cerebral amyloid angiopathy, with the disease-causing *APP* variants generally located inside or surrounding the Aβ domain, resulting in dysregulated cleavage of the Aβ peptide (Greenberg et al., 2020). Three of these variants are located just within the neighbouring AICD: p.L723P, p.K724M, and p.K724N. The p.L723P variant was identified in an Australian individual with a family history of early-onset Alzheimer's disease (Kwok et al., 2000). Transfected Chinese Hamster Ovarian (CHO) cells with mutant APP p.L723P constructs exhibited almost 2-fold increase in the Aβ42/Aβ40 ratio, which drastically increases Alzheimer's disease risk. On the neighbouring lysine residue, two early-onset Alzheimer's disease variants were identified. The p.K724M variant was found in three early-onset Alzheimer's disease patients of a Chinese family. Similarly, transfection of plasmids containing mutant APP cDNA in HEK293 cells demonstrated a more than 2-fold increase in the Aβ42/Aβ40 ratio (Peng et al., 2014). The p.K724N variant was found in one individual of a Belgian family who presented with early-onset Alzheimer's disease and a positive family history of early-onset Alzheimer's disease. Again, transfection of mutant APP cDNA in HEK293T cells resulted in a near 3-fold increase in Aβ42/Aβ40 ratio (Theuns et al., 2006). The p.V742L variant reported in the current study is more C-terminal, i.e. more distant from the Aβ domain, and the patient has small vessel disease with mainly subcortical infarcts, not Alzheimer's disease. Therefore, we expect a different pathomechanism that is potentially related to AICD-exclusive functions.

5.2. AICD interactors regulate APP trafficking towards lysosomes

One of the processes regulated by the AICD is the subcellular localization of APP and we have demonstrated increased presence of APP in lysosomes in patient fibroblasts. Previous studies have identified AICD interactors that regulate APP internalization and endolysosomal sorting (Swaminathan et al., 2016). For example, the YTSI motif within the AICD interacts with AP-3 in a phosphorylation-dependent manner to direct APP trafficking to lysosomes (Tam et al., 2016). Also, several interactors of the YENPTY motif within AICD were previously found to regulate APP localization towards lysosomes. For example, Caster et al (Caster and Kahn, 2013). demonstrated in HeLa cells that APP p.Y757A (YENPTY) impairs the AICD to recruit Mint3, resulting in APP trafficking defects causing increased lysosomal sorting. Similarly, La Rosa et al (La Rosa et al., 2015). showed in mice that APP p.Y757G (YENPTY) disrupts the interaction between the AICD and sortilin-related receptor (SorLA) to cause increased presence of APP in lysosomes. In contrast to the data presented in the current study however, La Rosa et al (La Rosa et al., 2015). also observed altered APP localization in early endosomes, late endosomes, and Golgi. Altogether, these studies demonstrate that phosphorylation of motifs within the AICD regulate APP trafficking towards lysosomes by regulating AICD interactions. Therefore, we hypothesize that the APP p.V742L variant, which is adjacent to the T743 (VTPEER) phosphorylation site, affects such interactions to favour APP trafficking towards lysosomes. Future studies performing co-IP of APP combined with mass spectrometry should identify these interactors.

5.3. Lysosomal APP accumulation in patient fibroblasts does not induce lysosomal motility defects

Accumulation of APP in lysosomes can have detrimental effects on lysosomal functioning. Bretou et al (Bretou et al., 2024). reported endolysosomal maturation defects, impaired Ca^{2+} refilling, and decreased motility of lysosomes following accumulation of membrane-tethered APP C-terminal fragments, including the AICD. Surprisingly, we did not observe altered lysosomal motility in patient fibroblasts. This might be explained by the different approaches used. Bretou et al (Bretou et al., 2024). deployed PSEN1/PSEN2/APP knock-out mouse embryonic fibroblasts in which exogenous membrane-tethered AICD was introduced to achieve accumulation in lysosomes. We used human adult fibroblasts in which endogenous APP and C-terminal fragments accumulate in lysosomes. It can be hypothesized that endogenous APP accumulates in lysosomes to a lesser extent compared to overexpressed exogenous APP, which therefore may not be sufficient to induce lysosomal defects. Moreover, membrane-tethered AICD is functionally different from cleaved AICD (Deyts et al., 2012), which implies that accumulation of these different AICD forms may have different consequences.

5.4. Dysregulation of genes related to APP or ischemic strokes

Gene expression analysis demonstrated that highly differentially expressed genes in our dataset were related to APP or the vascular system, thus potentially relevant to the patient's ischemic cerebral small vascular disease. Interestingly, some of these genes encode proteins that interact with APP. Firstly, CCNG1 is a cell-cycle regulator that was earlier found to be upregulated in cerebral arteries of Alzheimer's disease mice and directly binds to APP (Badhwar et al., 2017). Secondly, UCHL1 interacts with APP to promote its degradation in lysosomes and has previously been linked to Alzheimer's disease and vascular permeability (Zhang et al., 2014; Mitra et al., 2021). We, however, report downregulation of UCHL1 in patient fibroblast, thus excluding UCHL1-mediated APP trafficking to lysosomes as a mechanism. Finally, TLN1 directly interacts with the AICD at the synapse to mechanically synchronize the pre- and post-synapse (Ellis et al., 2024). The earlier mentioned co-IP experiments that should be performed in future studies should identify if these proteins indeed undergo different interactions with APP p.V742L.

In addition to APP interactors, we observed differential expression of genes contributing to stroke risk. HSP90AA1 is highly expressed in brain, blood, and arteries and single nucleotide polymorphisms (SNPs) in HSP90AA1 are associated with stroke risk, likely through regulating interactions with transcription factors (Kobzeva et al., 2024). GDF15 was among the top 5 proteins with largest contribution to ischemic stroke risk score in a UK Biobank study (Gan et al., 2025). Finally, LAMC1 is suggested to increase stroke risk through regulating lipid levels (Surakka et al., 2023). These results suggest that the APP p.V742L variant indeed affects pathways related to APP and vessel functioning. However, future studies in more relevant cell types are needed to reveal the mechanism linking the variant to ischemic strokes. This could be performed by reprogramming patient-derived cells into induced pluripotent stem cells (iPSCs), followed by differentiation into neuronal cultures and more complex 3D assembloids that integrate both neuronal and vascular-like structures to better mimic the cerebrovascular phenotype in vitro (Takahashi et al., 2007; Kistemaker et al., 2025). These neuronal cells should also be deployed to study AICD-FE65 mediated gene expression, as T743 is phosphorylated specific for

neurons and regulates this interaction (Ramelot and Nicholson, 2001; Chang et al., 2006; Radzimanowski et al., 2008; Bukhari et al., 2016). Finally, as the current findings are based on one patient cell line, future studies should introduce the APP p.V742L variant in different genetic backgrounds using CRISPR/Cas9 to account for interindividual transcriptomic variance and overcome the current $n = 1$ limitation.

5.5. Enhanced affinity of APP p.V742L for FE65

As the AICD regulates gene transcription through interacting with FE65 and TIP60, we hypothesized that the altered transcriptome in patient fibroblasts results from an effect of the APP p.V742L variant on this interaction (Cao and Südhof, 2001; Probst et al., 2020). Indeed, we have shown increased affinity of APP p.V742L for FE65, providing a mechanistic link between the variant and the observed changes in gene transcription in patient fibroblasts. Although FE65 binds to the YENPTY motif more C-terminal in the AICD, the VTPEER motif is described to regulate this interaction. For instance, 14–3-3ɣ binding to the VTPEER motif greatly enhances FE65-dependent gene transactivation (Sumioka et al., 2005). Furthermore, phosphorylation status of the threonine residue within the VTPEER motif is an important determinant of FE65 binding to the YENPTY motif (Chang et al., 2006), indicating that a variant within the VTPEER motif could interfere with FE65 binding to the AICD. To confirm that the altered interaction between the AICD and FE65 observed here indeed is the underlying source of dysregulated gene transcription, future studies should investigate the formation of transcriptionally-active AICD-FE65-TIP60 complexes in the nucleus in patient cells by for example immunocytochemistry (Cao and Südhof, 2001). Considering the cerebral manifestations of the patient's symptoms, this experiment should ideally be performed in the earlier mentioned iPSC-derived neuronal cells, which exhibit the neuron-specific phosphorylation of T743 in the VTPEER motif (Iijima et al., 2000).

To summarize, our data shows impairment of critical AICD functions resulting from the APP p.V742L variant. We have demonstrated increased APP trafficking towards lysosomes, dysregulated gene transcription, and enhanced affinity of the AICD for its most important interactor FE65. Further studies should focus on how the AICD variant induces ischemic strokes in more relevant models. This will not only assist in elucidating disease mechanisms behind the patients ischemic strokes, but will also generate fundamental insights into the function of the AICD in the brain.

Supplementary data to this article can be found online at https://doi.org/10.1016/j.nbd.2026.107280.

CRediT authorship contribution statement

Bas J.B. Voesenek: Writing – review & editing, Writing – original draft, Visualization, Validation, Software, Methodology, Investigation, Formal analysis, Data curation. **Julie W. Rutten:** Writing – review & editing, Supervision, Investigation. **Monique P.C. Mulder:** Writing – review & editing, Writing – original draft, Resources, Methodology. **Hailiang Mei:** Writing – review & editing, Writing – original draft, Methodology, Investigation, Formal analysis, Data curation. **Esther A. R. Nibbeling:** Writing – review & editing, Writing – original draft, Methodology, Investigation, Formal analysis. **Ellis S. van Etten:** Writing – review & editing, Writing – original draft, Investigation. **Willeke M.C. van Roon-Mom:** Writing – review & editing, Supervision, Resources, Project administration, Conceptualization. **Saskia A.J. Lesnik Oberstein:** Writing – review & editing, Writing – original draft, Supervision, Resources, Project administration, Funding acquisition, Conceptualization. **Elena Daoutsali:** Writing – review & editing, Supervision, Methodology, Funding acquisition, Conceptualization. **Ronald A.M. Buijsen:** Writing – review & editing, Supervision, Project administration, Methodology, Funding acquisition, Conceptualization.

Ethical approval

This study was approved by the LUMC scientific ethical committee and written informed consent was obtained from the APP p.V742L patient and unaffected individuals.

Funding

R.A.M.B., E.D., S.A.J.L.O., and W.V.R.M. received funding from the Sargenti Medical Research Fund (Leiden University Fund grant W225008-2-78). S.A.J.L.O. has financial research support from the Netherlands Organisation for Health Research and Development (ZonMW grant 91717325) and the Netherlands Brain Foundation (grant HA2016-02-03). M.P.C.M. acknowledges financial support from the Dutch Research Council (NWO VIDI grant VI.VIDI.213.110).

Declaration of competing interest

The authors declare that they have no known competing financial interests or personal relationships that could have appeared to influence the work reported in this paper.

Acknowledgements

We thank the APP p.V742L patient for providing a skin biopsy and sharing clinical data to support this research. We also thank her daughter and other family members for sharing their clinical data. We thank the SCA1 Giving Circle for providing control fibroblast lines. Finally, we thank Cami Talavera Ormeño (Peptide Facility, Department of Cell and Chemical Biology, LUMC, Leiden, Netherlands) for support on synthesizing the AICD peptides. Figures were created with the help of BioRender.com.

Data availability

The RNA-seq data that support the findings of this study are available upon request in the Genome-Phenome Archive (EGAD50000001825). The authors confirm that the data supporting the findings of this study are available within the article and its supplementary material.

References

Abe, R.J., Savage, H., Imanishi, M., et al., 2020. p90RSK-MAGI1 module controls endothelial permeability by post-translational modifications of MAGI1 and hippo pathway. Front. Cardiovasc. Med. 7, 542485. https://doi.org/10.3389/fcvm.2020.542485.

Ahn, B.Y., Jeong, Y., Kim, S., et al., 2023 Jan. Cdon suppresses vascular smooth muscle calcification via repression of the Wnt/Runx2 Axis. Exp. Mol. Med. 55 (1), 120–131. https://doi.org/10.1038/s12276-022-00909-7.

Astillero-Lopez, V., Villar-Conde, S., Gonzalez-Rodriguez, M., et al., 2024 Jul. Proteomic analysis identifies HSP90AA1, PTK2B, and ANXA2 in the human entorhinal cortex in Alzheimer's disease: potential role in synaptic homeostasis and aβ pathology through microglial and astroglial cells. Brain Pathol. 34 (4), e13235. https://doi.org/10.1111/bpa.13235.

Badhwar, A., Brown, R., Stanimirovic, D.B., Haqqani, A.S., Hamel, E., 2017 Mar. Proteomic differences in brain vessels of Alzheimer's disease mice: normalization by PPARγ agonist pioglitazone. J. Cereb. Blood Flow Metab. 37 (3), 1120–1136. https://doi.org/10.1177/0271678x16655172.

Bergström, S., Remnestål, J., Yousef, J., et al., 2021 Jul. Multi-cohort profiling reveals elevated CSF levels of brain-enriched proteins in Alzheimer's disease. Ann. Clin. Transl. Neurol. 8 (7), 1456–1470. https://doi.org/10.1002/acn3.51402.

Bonaterra-Pastra, A., Solé, M., Lope-Piedrafita, S., et al., 2024 Jul 29. The presence of circulating human apolipoprotein J reduces the occurrence of cerebral microbleeds in a transgenic mouse model with cerebral amyloid angiopathy. Alzheimer's Res. Ther. 16 (1), 169. https://doi.org/10.1186/s13195-024-01541-5.

Bretou, M., Sannerud, R., Escamilla-Ayala, A., et al., 2024 Jun 17. Accumulation of APP C-terminal fragments causes endolysosomal dysfunction through the dysregulation of late endosome to lysosome-ER contact sites. Dev. Cell 59 (12), 1571–1592 e9. https://doi.org/10.1016/j.devcel.2024.03.030.

Buga, A.M., Margaritescu, C., Scholz, C.J., Radu, E., Zelenak, C., Popa-Wagner, A., 2014. Transcriptomics of post-stroke angiogenesis in the aged brain. Front. Aging Neurosci. 6, 44. https://doi.org/10.3389/fnagi.2014.00044.

Buijsen, R.A.M., Hu, M., Sáez-González, M., et al., 2023 Aug. Spinocerebellar Ataxia type 1 characteristics in patient-derived fibroblast and iPSC-derived neuronal cultures. Mov. Disord. 38 (8), 1428–1442. https://doi.org/10.1002/mds.29446.
Bukhari, H., Kolbe, K., Leonhardt, G., et al., 2016 Nov. Membrane tethering of APP c-terminal fragments is a prerequisite for T668 phosphorylation preventing nuclear sphere generation. Cell. Signal. 28 (11), 1725–1734. https://doi.org/10.1016/j.cellsig.2016.08.007.
Bycroft, C., Freeman, C., Petkova, D., et al., 2018 Oct. The UK biobank resource with deep phenotyping and genomic data. Nature 562 (7726), 203–209. https://doi.org/10.1038/s41586-018-0579-z.
Cao, X., Südhof, T.C., 2001 Jul 6. A transcriptionally [correction of transcriptively] active complex of APP with Fe65 and histone acetyltransferase Tip60. Science 293 (5527), 115–120. https://doi.org/10.1126/science.1058783.
Caster, A.H., Kahn, R.A., 2013 Oct 4. Recruitment of the Mint3 adaptor is necessary for export of the amyloid precursor protein (APP) from the Golgi complex. J. Biol. Chem. 288 (40), 28567–28580. https://doi.org/10.1074/jbc.M113.481101.
Chang, K.A., Kim, H.S., Ha, T.Y., et al., 2006 Jun. Phosphorylation of amyloid precursor protein (APP) at Thr668 regulates the nuclear translocation of the APP intracellular domain and induces neurodegeneration. Mol. Cell. Biol. 26 (11), 4327–4338. https://doi.org/10.1128/mcb.02393-05.
Cho, Y., Bae, H.G., Okun, E., Arumugam, T.V., Jo, D.G., Jul 2022. Physiology and pharmacology of amyloid precursor protein. Pharmacol. Ther. 235, 108122. https://doi.org/10.1016/j.pharmthera.2022.108122.
Danzi, M.C., Dohrn, M.F., Fazal, S., et al., 2023 Jul 13. Deep structured learning for variant prioritization in mendelian diseases. Nat. Commun. 14 (1), 4167. https://doi.org/10.1038/s41467-023-39306-7.
Deyts, C., Vetrivel, K.S., Das, S., et al., 2012 Feb 1. Novel GαS-protein signaling associated with membrane-tethered amyloid precursor protein intracellular domain. J. Neurosci. 32 (5), 1714–1729. https://doi.org/10.1523/jneurosci.5433-11.2012.
Ellis, C., Ward, N.L., Rice, M., et al., 2024 Nov. The structure of an amyloid precursor protein/Talin complex indicates a mechanical basis of Alzheimer's disease. Open Biol. 14 (11), 240185. https://doi.org/10.1098/rsob.240185.
Ershov, D., Phan, M.S., Pylvänäinen, J.W., et al., 2022 Jul. TrackMate 7: integrating state-of-the-art segmentation algorithms into tracking pipelines. Nat. Methods 19 (7), 829–832. https://doi.org/10.1038/s41592-022-01507-1.
Esteve, P., Sandonìs, A., Cardozo, M., et al., 2011 May. SFRPs act as negative modulators of ADAM10 to regulate retinal neurogenesis. Nat. Neurosci. 14 (5), 562–569. https://doi.org/10.1038/nn.2794.
Fessner, A., Esser, J.S., Bluhm, F., et al., 2014 Feb 1. The transcription factor HoxB5 stimulates vascular remodelling in a cytokine-dependent manner. Cardiovasc. Res. 101 (2), 247–255. https://doi.org/10.1093/cvr/cvt244.
Fokkema, I., Kroon, M., López Hernández, J.A., et al., 2021 Dec. The LOVD3 platform: efficient genome-wide sharing of genetic variants. Eur. J. Hum. Genet. 29 (12), 1796–1803. https://doi.org/10.1038/s41431-021-00959-x.
Gan, X., Yang, S., Zhang, Y., et al., 2025 Feb. Large-scale plasma proteomics profiles for predicting ischemic stroke risk in the general population. Stroke 56 (2), 456–464. https://doi.org/10.1161/strokeaha.124.048654.
Glienke, J., Sturz, A., Menrad, A., Thierauch, K.H., 2002 Dec. CRIM1 is involved in endothelial cell capillary formation in vitro and is expressed in blood vessels in vivo. Mech. Dev. 119 (2), 165–175. https://doi.org/10.1016/s0925-4773(02)00355-6.
Greenberg, S.M., Bacskai, B.J., Hernandez-Guillamon, M., Pruzin, J., Sperling, R., van Veluw, S.J., 2020 Jan. Cerebral amyloid angiopathy and Alzheimer disease - one peptide, two pathways. Nat. Rev. Neurol. 16 (1), 30–42. https://doi.org/10.1038/s41582-019-0281-2.
Gueniot, F., Rubin, S., Bougaran, P., et al., 2022 Apr. Targeting Pdzrn3 maintains adult blood-brain barrier and central nervous system homeostasis. J. Cereb. Blood Flow Metab. 42 (4), 613–629. https://doi.org/10.1177/0271678x211048981.
Haass, C., Kaether, C., Thinakaran, G., Sisodia, S., 2012 May. Trafficking and proteolytic processing of APP. Cold Spring Harb. Perspect. Med. 2 (5), a006270. https://doi.org/10.1101/cshperspect.a006270.
Hartmann, S., Yasmeen, S., Jacobs, B.M., et al., 2023 Oct 12. ADRA2A and IRX1 are putative risk genes for Raynaud's phenomenon. Nat. Commun. 14 (1), 6156. https://doi.org/10.1038/s41467-023-41876-5.
Hu, D., Dong, X., Wang, Q., et al., 2023. PCP4 promotes Alzheimer's disease pathogenesis by affecting amyloid-β protein precursor processing. J. Alzheimer's Dis 94 (2), 737–750. https://doi.org/10.3233/jad-230192.
Hu, X., Dong, J., Geng, P., et al., 2024 Jun. Nicotine treatment ameliorates blood-brain barrier damage after acute ischemic stroke by regulating endothelial scaffolding protein Pdlim5. Transl. Stroke Res. 15 (3), 672–687. https://doi.org/10.1007/s12975-023-01158-0.
Iijima, K., Ando, K., Takeda, S., et al., 2000 Sep. Neuron-specific phosphorylation of Alzheimer's beta-amyloid precursor protein by cyclin-dependent kinase 5. J. Neurochem. 75 (3), 1085–1091. https://doi.org/10.1046/j.1471-4159.2000.0751085.x.
Karczewski, K.J., Francioli, L.C., Tiao, G., et al., 2020 May. The mutational constraint spectrum quantified from variation in 141,456 humans. Nature 581 (7809), 434–443. https://doi.org/10.1038/s41586-020-2308-7.
Katusic, Z.S., d'Uscio, L.V., He, T., 2025 Sep 5. Cerebrovascular protective functions of amyloid precursor protein: progress and therapeutic prospects. Pharmacol. Ther. 275, 108921. https://doi.org/10.1016/j.pharmthera.2025.108921.
Kim, Y.M., Park, S., Choi, S.Y., et al., 2022 Oct. Clusterin binding modulates the aggregation and neurotoxicity of amyloid-β(1-42). Mol. Neurobiol. 59 (10), 6228–6244. https://doi.org/10.1007/s12035-022-02973-6.
King, A., Szekely, B., Calapkulu, E., et al., 2020 Jul 31. The increased densities, but different distributions, of both C3 and S100A10 Immunopositive astrocyte-like cells in Alzheimer's disease brains suggest possible roles for both A1 and A2 astrocytes in the disease pathogenesis. Brain Sci. 10 (8). https://doi.org/10.3390/brainsci10080503.
Kistemaker, L., van Bodegraven, E.J., de Vries, H.E., Hol, E.M., 2025 Jun. Vascularized human brain organoids: current possibilities and prospects. Trends Biotechnol. 43 (6), 1275–1285. https://doi.org/10.1016/j.tibtech.2024.11.021.
Kobzeva, K., Ivenkov, M., Gromov, R., Bushueva, O., 2024 Dec 11. HSP90 family members, their regulators and ischemic stroke risk: a comprehensive molecular-genetics and bioinformatics analysis. Front. Biosci. (Schol. Ed.). 16 (4), 19. https://doi.org/10.31083/j.fbs1604019.
Kwok, J.B., Li, Q.X., Hallupp, M., et al., 2000 Feb. Novel Leu723Pro amyloid precursor protein mutation increases amyloid beta42(43) peptide levels and induces apoptosis. Ann. Neurol. 47 (2), 249–253. https://doi.org/10.1002/1531-8249(200002)47:2<249::aid-ana18>3.0.co;2-8.
La Rosa, L.R., Perrone, L., Nielsen, M.S., Calissano, P., Andersen, O.M., Matrone, C., 2015. Y682G mutation of amyloid precursor protein promotes endo-lysosomal dysfunction by disrupting APP-SorLA interaction. Front. Cell. Neurosci. 9, 109. https://doi.org/10.3389/fncel.2015.00109.
Lee, M.S., Kao, S.C., Lemere, C.A., et al., 2003 Oct 13. APP processing is regulated by cytoplasmic phosphorylation. J. Cell Biol. 163 (1), 83–95. https://doi.org/10.1083/jcb.200301115.
Manousopoulou, A., Yuen, H.M., Sharp, M.M., et al., 2020 Jan. Quantitative proteomic profiling of white matter in cases of cerebral amyloid angiopathy reveals upregulation of extracellular matrix proteins and clusterin. Free Neuropathol. 1. https://doi.org/10.17879/freeneuropathology-2020-2955.
Mitra, S., Epshtein, Y., Sammani, S., et al., 2021 Apr 1. UCHL1, a deubiquitinating enzyme, regulates lung endothelial cell permeability in vitro and in vivo. Am. J. Phys. Lung Cell. Mol. Phys. 320 (4), L497–L507. https://doi.org/10.1152/ajplung.00492.2020.
Müller, U.C., Deller, T., Korte, M., 2017 May. Not just amyloid: physiological functions of the amyloid precursor protein family. Nat. Rev. Neurosci. 18 (5), 281–298. https://doi.org/10.1038/nrn.2017.29.
Ng, L.L., Chow, J., Lau, K.F., 2024 Dec 19. The AICD interactome: implications in neurodevelopment and neurodegeneration. Biochem. Soc. Trans. 52 (6), 2539–2556. https://doi.org/10.1042/bst20241510.
Peng, X.L., Hou, L., Xu, S.H., et al., 2014 Nov. Novel APP K724M mutation causes Chinese early-onset familial Alzheimer's disease and increases amyloid-β42 to amyloid-β40 ratio. Neurobiol. Aging 35 (11), 2657.e1–2657.e6. https://doi.org/10.1016/j.neurobiolaging.2014.06.005.
Piñero, J., Ramírez-Anguita, J.M., Saüch-Pitarch, J., et al., 2020 Jan 8. The DisGeNET knowledge platform for disease genomics: 2019 update. Nucleic Acids Res. 48 (D1), D845–D855. https://doi.org/10.1093/nar/gkz1021.
Probst, S., Krüger, M., Kägi, L., et al., 2020 Sep 8. Fe65 is the sole member of its family that mediates transcription regulated by the amyloid precursor protein. J. Cell Sci. 133 (17). https://doi.org/10.1242/jcs.242917.
Radzimanowski, J., Simon, B., Sattler, M., Beyreuther, K., Sinning, I., Wild, K., 2008. Structure of the intracellular domain of the amyloid precursor protein in complex with Fe65-PTB2. EMBO Rep. 9 (11), 1134–1140. https://doi.org/10.1038/embor.2008.188.
Ramelot, T.A., Nicholson, L.K., 2001 Mar 30. Phosphorylation-induced structural changes in the amyloid precursor protein cytoplasmic tail detected by NMR. J. Mol. Biol. 307 (3), 871–884. https://doi.org/10.1006/jmbi.2001.4535.
Sewduth, R.N., Kovacic, H., Jaspard-Vinassa, B., et al., 2017 Jan 31. PDZRN3 destabilizes endothelial cell-cell junctions through a PKCζ-containing polarity complex to increase vascular permeability. Sci. Signal. 10 (464). https://doi.org/10.1126/scisignal.aag3209.
Sherman, B.T., Hao, M., Qiu, J., et al., 2022 Jul 5. DAVID: a web server for functional enrichment analysis and functional annotation of gene lists (2021 update). Nucleic Acids Res. 50 (W1), W216–w221. https://doi.org/10.1093/nar/gkac194.
Shimoyama, T., Hiraoka, S., Takemoto, M., et al., 2010 Apr. CCN3 inhibits neointimal hyperplasia through modulation of smooth muscle cell growth and migration. Arterioscler. Thromb. Vasc. Biol. 30 (4), 675–682. https://doi.org/10.1161/atvbaha.110.203356.
Sumioka, A., Nagaishi, S., Yoshida, T., Lin, A., Miura, M., Suzuki, T., 2005 Dec 23. Role of 14-3-3gamma in FE65-dependent gene transactivation mediated by the amyloid beta-protein precursor cytoplasmic fragment. J. Biol. Chem. 280 (51), 42364–42374. https://doi.org/10.1074/jbc.M504278200.
Surakka, I., Wu, K.H., Hornsby, W., et al., 2023 Aug 9. Multi-ancestry meta-analysis identifies 5 novel loci for ischemic stroke and reveals heterogeneity of effects between sexes and ancestries. Cell Genom. 3 (8), 100345. https://doi.org/10.1016/j.xgen.2023.100345.
Swaminathan, G., Zhu, W., Plowey, E.D., 2016 Dec. BECN1/Beclin 1 sorts cell-surface APP/amyloid β precursor protein for lysosomal degradation. Autophagy 12 (12), 2404–2419. https://doi.org/10.1080/15548627.2016.1234561.
Szepanowski, L.P., Wruck, W., Kapr, J., et al., 2024 Mar 28. Cockayne syndrome patient iPSC-derived brain organoids and neurospheres show early transcriptional dysregulation of biological processes associated with brain development and metabolism. Cells 13 (7). https://doi.org/10.3390/cells13070591.
Takahashi, K., Tanabe, K., Ohnuki, M., et al., 2007 Nov 30. Induction of pluripotent stem cells from adult human fibroblasts by defined factors. Cell 131 (5), 861–872. https://doi.org/10.1016/j.cell.2007.11.019.
Tam, J.H., Cobb, M.R., Seah, C., Pasternak, S.H., 2016. Tyrosine binding protein sites regulate the intracellular trafficking and processing of amyloid precursor protein through a novel lysosome-directed pathway. PLoS One 11 (10), e0161445. https://doi.org/10.1371/journal.pone.0161445.
Tan, Z., Chen, K., Wu, W., et al., 2018. Overexpression of HOXC10 promotes angiogenesis in human glioma via interaction with PRMT5 and upregulation of

VEGFA expression. Theranostics 8 (18), 5143–5158. https://doi.org/10.7150/thno.27310.

Tervi, A., Ramste, M., Abner, E., et al., 2024 Sep 11. Genetic and functional analysis of Raynaud's syndrome implicates loci in vasculature and immunity. Cell Genom. 4 (9), 100630. https://doi.org/10.1016/j.xgen.2024.100630.

Theuns, J., Marjaux, E., Vandenbulcke, M., et al., 2006. Alzheimer dementia caused by a novel mutation located in the APP C-terminal intracytosolic fragment. Hum. Mutat. 27 (9), 888–896. https://doi.org/10.1002/humu.20402.

Uhlén, M., Fagerberg, L., Hallström, B.M., et al., 2015 Jan 23. Proteomics. Tissue-based map of the human proteome. Science 347 (6220), 1260419. https://doi.org/10.1126/science.1260419.

Vogrinc, D., Gregorič Kramberger, M., Emeršič, A., Čučnik, S., Goričar, K., Dolžan, V., 2023 Jan 29. Genetic polymorphisms in oxidative stress and inflammatory pathways as potential biomarkers in Alzheimer's disease and dementia. Antioxidants (Basel) 12 (2). https://doi.org/10.3390/antiox12020316.

Wojtas, A.M., Kang, S.S., Olley, B.M., et al., 2017 Aug 15. Loss of clusterin shifts amyloid deposition to the cerebrovasculature via disruption of perivascular drainage pathways. Proc. Natl. Acad. Sci. USA 114 (33), E6962–e6971. https://doi.org/10.1073/pnas.1701137114.

Yang, Y., Chen, H., Huang, S., et al., 2025 Feb 3. BOK-engaged mitophagy alleviates neuropathology in Alzheimer's disease. Brain 148 (2), 432–447. https://doi.org/10.1093/brain/awae241.

Zhang, M., Cai, F., Zhang, S., Zhang, S., Song, W., 2014 Dec 3. Overexpression of ubiquitin carboxyl-terminal hydrolase L1 (UCHL1) delays Alzheimer's progression in vivo. Sci. Rep. 4, 7298. https://doi.org/10.1038/srep07298.

Zhang, F., Gannon, M., Chen, Y., Zhou, L., Jiao, K., Wang, Q., 2017 Oct. The amyloid precursor protein modulates α(2A)-adrenergic receptor endocytosis and signaling through disrupting arrestin 3 recruitment. FASEB J. 31 (10), 4434–4446. https://doi.org/10.1096/fj.201700346R.

Zhao, X., Yang, J., Yang, C., 2022. The neuronal transcription factor Creb3l1 potential upregulates Ntrk2 in the hypertensive microenvironment to promote vascular smooth muscle cell-neuron interaction and prevent neurons from ferroptosis: a bioinformatic research of scRNA-seq data. Dis. Markers 2022, 8339759. https://doi.org/10.1155/2022/8339759.